Absorption lines from magnetically driven winds in X-ray binaries

S. Chakravorty, P. -O. Petrucci, J. Ferreira, G. Henri, R. Belmont, M. Clavel, S. Corbel, J. Rodriguez, M. Coriat, S. Drappeau, et al.

▶ **To cite this version:**

S. Chakravorty, P. -O. Petrucci, J. Ferreira, G. Henri, R. Belmont, et al.. Absorption lines from magnetically driven winds in X-ray binaries. Astronomy and Astrophysics - A&A, 2016, 589, 10.1051/0004-6361/201527163 . insu-03670249

HAL Id: insu-03670249

https://insu.hal.science/insu-03670249

Submitted on 17 May 2022

HAL is a multi-disciplinary open access archive for the deposit and dissemination of scientific research documents, whether they are published or not. The documents may come from teaching and research institutions in France or abroad, or from public or private research centers.

L'archive ouverte pluridisciplinaire **HAL**, est destinée au dépôt et à la diffusion de documents scientifiques de niveau recherche, publiés ou non, émanant des établissements d'enseignement et de recherche français ou étrangers, des laboratoires publics ou privés.

A&A 589, A119 (2016)
DOI: 10.1051/0004-6361/201527163
© ESO 2016

Astronomy & Astrophysics

Absorption lines from magnetically driven winds in X-ray binaries

S. Chakravorty[1,2], P.-O. Petrucci[1,2], J. Ferreira[1,2], G. Henri[1,2], R. Belmont[3,4], M. Clavel[5], S. Corbel[5], J. Rodriguez[5], M. Coriat[3,4], S. Drappeau[3,4], and J. Malzac[3,4]

[1] Université Grenoble Alpes, IPAG, 38000 Grenoble, France
e-mail: susmita.chakravorty@obs.ujf-grenoble.fr
[2] CNRS, IPAG, 38000 Grenoble, France
[3] Université de Toulouse, UPS-OMP, IRAP, 31028 Toulouse, France
[4] CNRS, IRAP, 9 Av. colonel Roche, 31028 Toulouse, France
[5] Laboratoire AIM (CEA/IRFU – CNRS/INSU – Université Paris Diderot), CEA DSM/IRFU/SAp, 91191 Gif-sur-Yvette, France

Received 11 August 2015 / Accepted 23 December 2015

ABSTRACT

Context. High resolution X-ray spectra of black hole X-ray binaries (BHBs) show blueshifted absorption lines suggesting the presence of outflowing winds. Furthermore, observations show that the disk winds are equatorial and they occur in the Softer (disk dominated) states of the outburst and are less prominent or absent in the Harder (power-law dominated) states.
Aims. We want to test whether the self-similar magneto-hydrodynamic (MHD) accretion-ejection models can explain the observational results for accretion disk winds in BHBs. In our models, the density at the base of the outflow from the accretion disk is not a free parameter. This mass loading is determined by solving the full set of dynamical MHD equations without neglecting any physical term. Thus, the physical properties of the outflow depend on and are controlled by the global structure of the disk.
Methods. We studied different MHD solutions characterized by different values of the disk aspect ratio (ε) and the ejection efficiency (p). We also generate two kinds of MHD solutions depending on the absence (cold solution) or presence (warm solution) of heating at the disk surface. Such heating could be either from dissipation of energy due to MHD turbulence in the disk or from illumination of the disk surface. Warm solutions can have large (>0.1) values of p, which would imply larger wind mass loading at the base of the outflow. We use each of these MHD solutions to predict the physical parameters (distance, density, velocity, magnetic field, etc.) of an outflow. Motivated by observational results, we have put limits on the ionization parameter (ξ), column density, and timescales. Further constraints were derived for the allowed values of ξ from thermodynamic instability considerations, particularly for the Hard SED. These physical constraints were imposed on each of these outflows to select regions within it, which are consistent with the observed winds.
Results. The cold MHD solutions are found to be inadequate and cannot account for winds because of their low ejection efficiency. On the contrary, warm solutions can have sufficiently high values of $p(\gtrsim 0.1)$, which are required to explain the observed physical quantities in the wind. From our thermodynamic equilibrium curve analysis for the outflowing gas, we find that in the Hard state a range of ξ is unstable. This constraint makes it impossible to have any wind at all in the Hard state.
Conclusions. Using the MHD outflow models we are able to explain the observed trends, i.e. that the winds are equatorial and that they are observable in the Soft states (and not expected in the Hard state) of the BHB outbursts.

Key words. magnetohydrodynamics (MHD) – X-rays: binaries – stars: black holes – stars: winds, outflows – atomic processes – accretion, accretion disks

1. Introduction

The launch of *Chandra* and *XMM-Newton* revealed blueshifted absorption lines in the high resolution X-ray spectra of stellar mass black holes in binaries (BHBs). These lines are signatures of winds from the accretion disk around the black hole. The velocity and ionization state of the gas interpreted from the absorption lines vary from object to object and from observation to observation. In most cases, only H- and He-like Fe ions are detected (e.g. Lee et al. 2002; Neilsen & Lee 2009, for GRS 1915+105; Miller et al. 2004, for GX 339-4; Miller et al. 2006, for H1743-322; and King et al. 2012, for IGR J17091-3624). In some of the objects, however, a wider range of ions is seen from O through Fe (e.g. Ueda et al. 2009, for GRS 1915+105; Miller et al. 2008; Kallman et al. 2009 for GRO J1655–40). The variations in the wind properties seem to indicate variations in the temperature, pressure, and density of the gas from one object to another. Furthermore, even in the same object, the winds seem to have variations depending on the accretion state of the black hole.

Both spectral and timing observations of most BHBs show common behaviour patterns centred around a few states of accretion. The spectral energy distributions (SEDs) corresponding to the different states have varying degrees of contribution from the accretion disk and the non-thermal power-law components. The X-ray studies of BHBs show that winds are not present in all states. It has been shown by several authors that the absorption lines are more prominent in the Softer (accretion disk dominated) states (Miller et al. 2008; Neilsen & Lee 2009; Blum et al. 2010; Ponti et al. 2012). For some objects, these changes are attributed to changes in the photoionizing flux (e.g. Miller et al. 2012, in the case of H1743-322). However, the alternative

explanation of "changes in the driving mechanism" is of greater relevance to this paper.

The observable properties of the accretion disk winds are often used to infer the driving mechanism of the winds (Lee et al. 2002; Ueda et al. 2009, 2010; Neilsen et al. 2011; Neilsen & Homan 2012). Hence the variation or disappearance of the wind through the various states of the BHB, has been interpreted as a variation in the driving mechanism of the wind. A good example is the case of GRO J1655–40. A well-known *Chandra* observation of GRO J1655–40 (Miller et al. 2006, 2008; Kallman et al. 2009) shows a rich absorption line spectrum from OVIII–NiXXVI, and has led the authors to the conclusion of a magnetic driving mechanism for the wind. Neilsen & Homan (2012) have analysed the data from another observation for the same source taken three weeks later and found absorption by Fe XXVI only. They argue that such a change cannot be due to variation in photoionization flux only and suggest that variable thermal pressure and magnetic fields may be important in driving long-term changes in the wind in GRO J1655–40.

In order to have a consolidated picture of these systems, it is necessary to understand the relation between the accretion states of the BHBs and the driving mechanisms of the winds. In this paper we investigate the magneto-hydrodynamic (hereafter MHD) solutions as driving mechanisms for winds from the accretion disks around BHBs: cold solutions from Ferreira (1997, hereafter F97) and warm solutions from Casse & Ferreira (2000b) and Ferreira (2004). To understand the basic motivation of the MHD solutions used to model the winds throughout this paper, it is important to discuss the distinction between winds and jets from accretion disks. Observationally, jets are usually described as collimated, fast (mildly relativistic) outflows detected or directly imaged in radio wavelengths. On the other hand, winds are detected as absorption features, showing speeds of a few thousand km s^{-1}. However, from a theoretical point of view, both are outflows launched from the accretion disk surface as a result of magnetic and/or thermal/radiative effects. The power carried by these outflows is, ultimately, a fraction of the released accretion power. Hence, although observationally distinct, theoretically, it is not easy to distinguish between the two. One way to make a clear theoretical distinction between these two outflows is to look at the magnetization σ at the disk surface, namely the ratio of the MHD Poynting flux to the sum of the thermal energy flux and the kinetic energy flux. Jets would have $\sigma > 1$, a high magnetization translating into both large asymptotic speeds and magnetic self-confinement. On the contrary, winds would be much less magnetized ($\sigma < 1$) with much lower asymptotic speeds and the confinement (if any) will come only from the external medium.

Magneto-hydrodynamic solutions have been used by other authors to address outflows in various systems. Of particular relevance to this paper are the works presented by Fukumura et al. (2010a,b, 2014, 2015). Based on the self-similar Contopoulos & Lovelace (1994) MHD models of outflowing material, these papers have already argued in favour of large-scale magneto-centrifugally driven winds in active galactic nuclei (AGNs; galaxies that host actively mass accreting super-massive black holes, $M_{\rm BH} > 10^6\ M_\odot$, at their centres). Their analysis shows that such models can account for the observed warm absorbers and ultra-fast outflows seen as absorption lines in high resolution X-ray spectra of AGN. They have also attempted to explain the broad absorption lines (seen in high resolution ultraviolet spectra of AGN) using the same MHD wind models. We note, however, that the Contopoulos & Lovelace (1994) model (which is an extension of the Blandford & Payne 1982 hydromagnetic flows) does not treat the underlying disk. As a consequence, the link between the mass loss in winds and the disk accretion rate is lost and the mass loading at the base of the disk can be almost arbitrarily large or small. On the contrary, the MHD models in F97 (and subsequent papers) link the density of the outflowing material to the disk accretion rate.

A consistent theory of MHD outflows from the disk must explain how much matter from the disk is deviated from the radial to the vertical motion, as well as the amount of energy and angular momentum carried away from the disk. This requires a thorough treatment of the resistive disk interior and matching it with the outflowing material using ideal MHD. The only way to solve such an entangled problem is to take into account all dynamical terms, a task that was done within a self-similar framework in F97.

The F97 MHD solutions have been used in Ferreira et al. (2006) and Petrucci et al. (2010), to describe accretion disks giving rise to jets in the Hard States of BHBs. Winds, on the other hand are seen in the Soft state of the BHBs when radio jets are absent. Using the F97 models we test whether the same theoretical framework (which can reproduce jets) can reproduce the observed properties of the winds (ionization parameter, column density, velocity, etc.). We shall also look into the parameter space of the theoretical models to distinguish between the Softer accretion states when the wind is observed and the Harder states when the absorption lines from the wind is not observed.

2. MHD accretion disk wind solutions

2.1. General properties

We use the F97 solutions that describe steady-state, axisymmetric solutions under the following two conditions:

(1) A large-scale magnetic field of bipolar topology is assumed to thread the accretion disk. The strength of the required vertical magnetic field component is obtained as a result of the solution (Ferreira 1995).
(2) Some anomalous turbulent resistivity is at work, allowing the plasma to diffuse through the field lines inside the disk.

For a set of disk parameters, the solutions are computed from the disk mid-plane to the asymptotic regime; the outflowing material becomes first super slow-magnetosonic, then Alfvénic, and finally fast-magnetosonic. All solutions that are discussed in this paper have this same asymptotic behaviour, which corresponds to the following physical scenario: after an opening of the radius of the outflow that leads to a very efficient acceleration of the plasma, the outflow undergoes a refocusing towards the axis (recollimation). The solutions are then mathematically terminated (see F97 for more details). Physically speaking, however, the outflowing plasma most probably undergoes an oblique shock (which is independent of the assumption concerning the thermal state of the magnetic surfaces) after the recollimation happens. However, theoretically accounting for the oblique shock is beyond the scope of this paper. Thus, in this paper we rely only on those solutions that cross their Alfvén surfaces before recollimating (i.e. before the solutions have to be mathematically terminated).

2.2. Model parameters

The rigorous mathematical details of how the isothermal MHD solutions for the accretion disk outflow are obtained are

given in the above-mentioned papers and we refrain from repeating them here. In this section we focus on describing the two parameters that affect the density n^+ (or ρ^+) of the outflowing material at a given radius r in the disk.

Because of ejection, the disk accretion rate varies with the radius even in a steady state, namely $\dot{M}_{\rm acc} \propto r^p$. This radial exponent, p (labelled ξ in F97, Ferreira et al. 2006; Petrucci et al. 2010, etc.) is very important since it measures the local ejection efficiency. For an accretion disk that is giving rise to an outflow, the mass outflow rate is related to the accretion rate through the ejection index p. If the disk extends between the inner radius $r_{\rm in}$ and the outer radius $r_{\rm out}$ and is being fed by a disk accretion rate $\dot{M}_{\rm acc}(r_{\rm out})$, the ejection to accretion mass rate ratio is

$$\frac{2\dot{M}_{\rm outflow}}{\dot{M}_{\rm acc}(r_{\rm out})} = 1 - \left(\frac{r_{\rm in}}{r_{\rm out}}\right)^p \simeq p \ln \frac{r_{\rm out}}{r_{\rm in}}, \quad (1)$$

where the last estimate holds only for $p \ll 1$. For the most extreme MHD solution discussed in this paper (namely $r_{\rm out} \simeq 10^7 r_{\rm in}$ and $p \simeq 0.1$), about 80% of the accreted mass is ejected in the form of the outflow. The larger the exponent, the more massive and slower is the outflow. Mass conservation writes

$$2\frac{{\rm d}\dot{M}_{\rm outflow}}{{\rm d}r} = 4\pi r \rho^+ u_z^+ = \frac{{\rm d}\dot{M}_{\rm acc}}{{\rm d}r} = p\frac{\dot{M}_{\rm acc}}{r}$$
$$n^+ m_{\rm p} = \rho^+ \simeq \frac{p}{\varepsilon}\frac{\dot{M}_{\rm acc}}{4\pi\Omega_{\rm K} r^3} \quad (2)$$

where $m_{\rm p}$ is the proton mass and the superscript "+" stands for the height where the flow velocity becomes sonic[1], namely $u_z^+ = C_{\rm s} = \Omega_{\rm K} h = \varepsilon V_{\rm K}$. Here, $V_{\rm K} = \Omega_{\rm K} r = \sqrt{GM_{\rm BH}/r}$ (where G is the gravitational constant) is the Keplerian speed and

$$\varepsilon = \frac{h}{r} \quad (3)$$

is the disk aspect ratio, where $h(r)$ is the vertical scale height at the cylindrical radius r. It can thus be seen that the wind density, a crucial quantity when studying absorption features, is mostly dependent on p and ε for a given disk accretion rate $\dot{M}_{\rm acc}$.

Equation (2) is the fundamental difference between the MHD models used in the previously mentioned papers by Fukumura et al. and the ones used in this work. While in the former, the initial wind density ρ^+ can be "arbitrarily" prescribed, i.e. independent of the underlying disk accretion rate, here it is a result of an accretion-ejection calculation and is determined by p and ε. In the Fukumura et al. papers there are two assumptions, put by hand, that determine the physical properties of the outflow. First, the authors do not use the parameter p. However, comparing the equations for the radial distributions of magnetic field ($B_z \propto r^{q-2}$) of the outflow, we can get the relation $q = \frac{3}{4} + \frac{p}{2}$ (Ferreira 1993). We note that q is not any parameter related to the accretion disk, but an index related to the outflow. The Fukumura et al. papers discuss two cases, $q = 1$ and $q = 3/4$, but for modelling the AGN winds they use the former, which would correspond to $p = 0.5$. The choice of $q = 1$ ensures that the density in the outflow followed $n \propto r^\alpha$ with $\alpha = 2q - 3 = 1$, as suggested by observations. Second, the density at the launching point of the wind is prescribed by a parameter η_W which is the ratio of the mass outflow rate to the disk accretion rate. We note that the authors use a constant value $\eta_W = 0.5$ independent of q. The fact that these pre-assigned values for the parameters define the outflow and that there is a lack of any connection to the accretion process, foster a sense of "physical arbitrariness". To achieve such a high value of η_W, an extra process (other than MHD acceleration) must be acting within the resistive disk (this is discussed in Sect. 5 in the context of Warm models).

[1] Here, the sonic speed only provides a convenient scaling for the velocity, especially in isothermal flows. In MHD winds, however, the critical speed that needs to be reached at the disk surface is the slow magnetosonic speed, which is always smaller than the sonic speed (see Appendix A for more details).

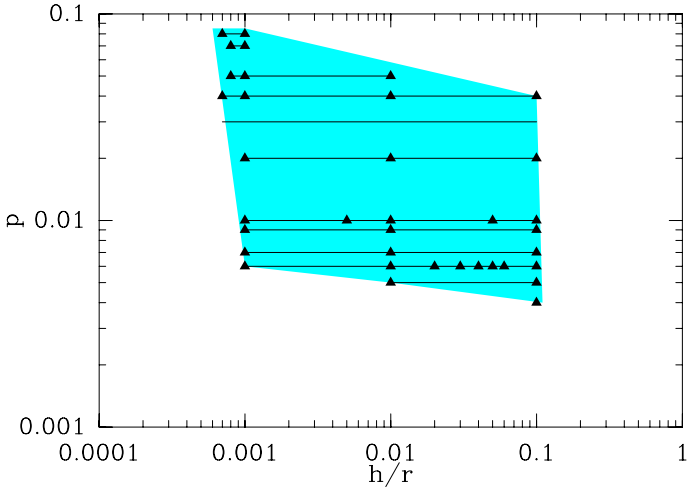

Fig. 1. Parameter space ejection index p ($\dot{M}_{\rm acc} \propto r^p$) versus disk aspect ratio $\varepsilon = h/r$ for isothermal, cold accretion-ejection solutions of F97. The coloured area shows the zone where super-Alfvénic outflows have been obtained, the triangles indicate some specific solutions, and lines are for constant p.

In the MHD models used in this paper the value of the exponent p influences the extent of magnetization in the outflow. This is another way in which the ejection index relates the accretion process and the outflow properties. In a non-relativistic framework, the ratio of the MHD Poynting flux to the kinetic energy flux at the disk surface is

$$\sigma^+ \simeq \frac{1}{p}\left(\frac{\Lambda}{1+\Lambda}\right). \quad (4)$$

(F97, Casse & Ferreira 2000a), where Λ is the ratio of the torque due to the outflow to the turbulent torque (usually referred to as the viscous torque). The torque due to the outflow transfers the disk angular momentum to the outflowing material, whereas the turbulent torque provides an outward radial transport within the disk. The smaller the value of p, the larger is the energy per unit mass in the outflow. A magnetically dominated self-confined outflow requires $\sigma^+ > 1$. The F97 outflow models have been obtained in the limit $\Lambda \to \infty$ so that the self-confined outflows carry away all the disk angular momentum and thereby rotational energy with $\sigma^+ \simeq 1/p \gg 1$. The outflow material reaches the maximum asymptotic poloidal speed $V_{\rm max} \sim V_{\rm K}(r_{\rm o})p^{-1/2}$, where $r_{\rm o}$ is the anchoring radius of the magnetic field line.

Figure 1 shows the $p - \varepsilon$ parameter space of super-Alfvénic MHD solutions obtained by F97 with cold, isothermal magnetic surfaces. It can be seen that under these assumptions it is impossible to achieve high values of $p \gtrsim 0.1$. Such a limit on the value of p does not improve, even if the magnetic surfaces are changed to be adiabatic, as long as the outflowing material remains cold (Casse & Ferreira 2000a). The outflow is cold when its enthalpy is negligible when compared to the magnetic energy, which is always verified in near Keplerian accretion disks. However, the warming up of the outflowing material could occur if some additional heat deposition becomes active at the disk surface layers

(through illumination for instance, or enhanced turbulent dissipation at the base of the corona). In that case, larger values of p up to ∼0.45 have been reported (Casse & Ferreira 2000b; Ferreira 2004). We will examine the cold outflows in Sect. 4 and the warm outflows in Sect. 5.

2.3. Scaling relationships

For the MHD outflow (with given ε and p) emitted from the accretion disk settled around a black hole, the important physical quantities are given at any cylindrical (r, z) by

$$n(r,z) = \frac{\dot{m}}{\sigma_{\rm T} r_{\rm g}} \left(\frac{r}{r_{\rm g}}\right)^{(p-3/2)} f_n(y) \quad (5)$$

$$B_i(r,z) = \left(\frac{\mu_{\rm o} m_{\rm p} \dot{m} c^2}{\sigma_{\rm T} r_{\rm g}}\right)^{1/2} \left(\frac{r}{r_{\rm g}}\right)^{(-5/4+p/2)} f_{B_i}(y) \quad (6)$$

$$v_i(r,z) = c \left(\frac{r}{r_{\rm g}}\right)^{-1/2} f_{v_i}(y) \quad (7)$$

$$\tau_{\rm dyn}(r) = \frac{2\pi r_{\rm g}}{c} \left(\frac{r}{r_{\rm g}}\right)^{3/2} f_\tau(y) \quad (8)$$

where $\sigma_{\rm T}$ is the Thomson cross section, c the speed of light, $r_{\rm g} = GM_{\rm BH}/c^2$ the gravitational radius, $\mu_{\rm o}$ the vacuum magnetic permeability, $y = z/r$ the self-similar variable, and the functions $f_X(y)$ are provided by the solution of the full set of MHD equations. In the above expressions, n is the proton number density and we consider it to be $\sim n_{\rm H}$ (the Hydrogen number density); v_i (or B_i) is any component of the velocity (or magnetic field) and $\tau_{\rm dyn} = 1/{\rm div}\boldsymbol{V}$ (where $\boldsymbol{V}$ is the plasma velocity) is a measure of the dynamical time in the flow. The normalized disk accretion rate used in the above equations is defined by

$$\dot{m} = \frac{\dot{M}_{\rm acc}(r_{\rm g})\, c^2}{L_{\rm Edd}}, \quad (9)$$

where $L_{\rm Edd}$ is the Eddington luminosity.

We note that we use a steady state assumption for the accretion disk of a BHB, i.e. the variation of the accretion rate with the radius is assumed to be the same for the entire disk (same p and same normalization). This assumption is maintained from the innermost regions (a few $r_{\rm g}$) to the outer part of the disk where the disk wind becomes relevant (between 10^3–$10^4 r_{\rm g}$). We acknowledge that this is a simplistic picture since BHBs are outbursting systems where the accretion rate is obviously varying. So the accretion rate of the outer part of disk could be significantly different to the one in the inner part. However, taking this effect into account would require considering a detailed time evolution of the accretion mechanism through the different stages of the outburst, which is far beyond the scope of this paper. Hence, we perform our calculations within the aforementioned scientific framework.

3. Observational constraints

3.1. Spectral energy distributions for the Soft and Hard states

The SED of BHBs usually comprises two components: (1) a thermal component; and (2) a non-thermal power-law component with a photon spectrum $N(E) \propto E^{-\Gamma}$ (Remillard & McClintock 2006). The thermal component is believed to be the radiation from the inner accretion disk around the black hole, and is conventionally modelled with a multi-temperature blackbody often showing a characteristic temperature ($T_{\rm in}$) near 1 keV.

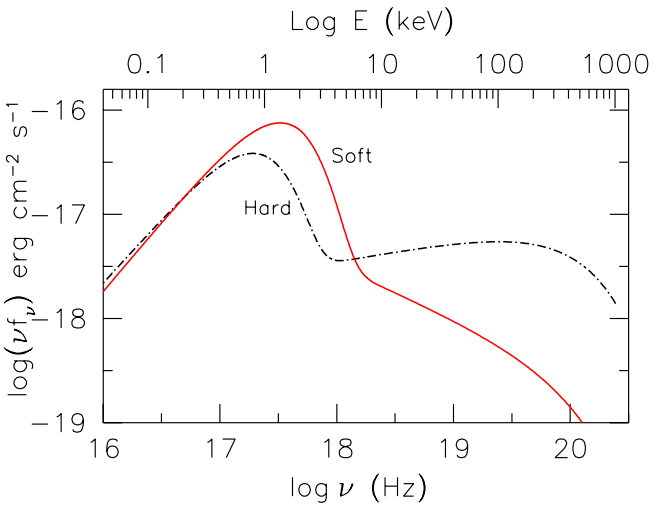

Fig. 2. SEDs corresponding to the Soft and Hard states of the outburst of a black hole of 10 $M_\odot$. The two important components of the SED, namely, the disk spectrum and the power-law have been added following the scheme described in Remillard & McClintock (2006). See Sect. 3.1 for the details.

During their outbursts the BHBs transition through different states where the SED shows varying degrees of contribution from the above-mentioned components. The state where the radiation from the inner accretion disk dominates and contributes more than 75% of the 2–20 keV flux is fiducially called the Soft state (Remillard & McClintock 2006). On the other hand, the fiducial Hard state is where the non-thermal power-law contributes more than 80% of the 2–20 keV flux (Remillard & McClintock 2006). For any given BHB, the accretion disk usually appears to be fainter and cooler in this Hard power-law state than it is in the Soft thermal state.

The radiation from a thin accretion disk can be modelled as the sum of local blackbodies emitted at different radii and the temperature $T_{\rm in}$ of the innermost annulus (with radius $r_{\rm in}$) of accreted matter is proportional to $\left[\dot{m}_{\rm obs}/(M_{\rm BH} r_{\rm in}^3)\right]^{1/4}$ (Peterson 1997; Frank et al. 2002), where the observational accretion rate $\dot{m}_{\rm obs}$ is defined as

$$\dot{m}_{\rm obs} = L_{\rm rad}/L_{\rm Edd}, \quad (10)$$

$L_{\rm rad}$ being the luminosity in the energy range 0.2 to 20 keV and $L_{\rm Edd}$ being the Eddington luminosity. A standard model for emission from a thin accretion disk is available as a disk blackbody (hereafter diskbb, Mitsuda et al. 1984; Makishima et al. 1987) in XSPEC[2] (Arnaud 1996). We use the diskbb in version 11.3 of XSPEC to generate the disk spectrum $f_{\rm disk}(\nu)$, where $T_{\rm in}$ is used as an input. The other required input for diskbb, the normalization, is proportional to $r_{\rm in}^2$. To $f_{\rm disk}(\nu)$ we add a hard power-law with a high energy cut-off, yielding

$$f(\nu) = f_{\rm disk}(\nu) + [A_{\rm pl}\nu^{-\alpha}] \exp^{-\frac{\nu}{\nu_{\rm max}}} \quad (11)$$

to account for the full SED. We use the high energy exponential cut-off to insert a break in the power-law at 100 keV.

We follow the prescription given in Remillard & McClintock (2006) to choose appropriate values of the relevant parameters to derive the two representative SEDs for a black hole of 10 $M_\odot$.

- *Soft state* (Fig. 2 solid red curve): in the Soft state the accretion disk extends all the way to $r_{\rm in} = 3R_{\rm s} = 6r_{\rm g}$. Thus

[2] http://heasarc.gsfc.nasa.gov/docs/xanadu/xspec/

$T_{\rm in} = 0.56$ keV. The power-law has $\Gamma = 2.5$ and $A_{\rm pl}$ is chosen in such a way that disk contributes to 80% of the 2–20 keV flux.

- *Hard state* (Fig. 2 dot-dashed black curve): with $r_{\rm in} = 6R_{\rm s} = 12r_{\rm g}$ we generate a cooler disk with $T_{\rm in} = 0.33$ keV. The power-law is dominant in this state with $\Gamma = 1.8$ so that 2–20 keV flux is only 20%.

For a 10 $M_\odot$ black hole, $L_{\rm Edd} = 1.23 \times 10^{39}$ erg s^{-1}. Using the above-mentioned fiducial SEDs, we can derive $\dot{m}_{\rm obs} = 0.14$ using the Soft SED and $\dot{m}_{\rm obs} = 0.07$ using the Hard SED. For simplicity, we assume $\dot{m}_{\rm obs} = 0.1$ for the rest of this paper.

It is important to note here the distinction between the disk accretion rate $\dot{m}$ (Eq. (9)) mentioned above, and the observed accretion rate $\dot{m}_{\rm obs}$, which is more commonly used in the literature. One can define

$$\dot{m} = \frac{2}{\eta_{\rm acc}} \frac{\dot{m}_{\rm obs}}{\eta_{\rm rad}}, \tag{12}$$

where the factor 2 is due to the assumption that we see only one of the two surfaces of the disk.

The accretion efficiency $\eta_{\rm acc} \simeq r_{\rm g}/2r_{\rm in}$ depends mostly on the black hole spin. For the sake of simplicity, we choose the Schwarzchild black hole, so that $\eta_{\rm acc} \sim 1/12$, both in Soft and Hard state.

The radiative efficiency, $\eta_{\rm rad} = 1$ if the inner accretion flow is radiatively efficient, i.e. it radiates away all the power released due to accretion. This is the case for a standard (i.e. geometrically thin, optically thick) accretion disk, and it is satisfied in the Soft state when the standard accretion disk extends all the way up to $r_{\rm in} = 6r_{\rm g}$. Thus $\dot{m} = 24\dot{m}_{\rm obs} = 2.4$. We acknowledge that $\eta_{\rm rad}$ can be expected to be <1 in the Hard state because the innermost parts of the accretion disk may be more complex. In the Hard state, part of the accretion power could be advected and not radiated (as it is in accretion dominated accretion flow, ADAF), or ejected (as in jet emitting disks, Ferreira et al. 2006). Instead of going into detailed calculations of such complex accretion disks, we accounted for the resultant modifications in the Hard SED by merely increasing the standard accretion disk radius $r_{\rm in}$ to $12r_{\rm g}$, keeping in mind that the inner part of the flow could be filled by a different, radiatively less efficient, accretion flow. However, $\eta_{\rm rad} < 1$ (in the Hard state), can be balanced by the fact that $\dot{m}_{\rm obs,\,Hard}$ is slightly smaller (0.07) than $\dot{m}_{\rm obs,\,Soft}$ (0.14), so that $\dot{m}_{\rm obs}/\eta_{\rm rad}$ remains the same for the Soft and the Hard states. Hence, for the sake of simplicity, we assume that the same value of $\dot{m} = 2.4$ can be retained for the Hard state.

3.2. Constraints from atomic physics

The MHD solutions can be used to predict the presence of outflowing material over a wide range of distances. For any given solution, this outflowing material spans wide ranges in physical parameters like ionization parameter, density, column density, velocity, and timescales. Only part of this outflow will be detectable through absorption lines; we refer to this part as the "detectable wind".

The ionization parameter is one of the key physical parameters when determining which region of the outflow can form a wind. There are several forms of ionization parameter in the literature. In this paper we use the definition most commonly used by X-ray high resolution spectroscopists, namely $\xi = L_{\rm ion}/(n_{\rm H}R^2_{\rm sph})$ (Tarter et al. 1969), where $L_{\rm ion}$ is the luminosity of the ionizing light in the energy range 1–1000 Rydberg (1 Rydberg = 13.6 eV) and $n_{\rm H}$ is the density of the gas located at a distance of $R_{\rm sph}$. We assume that at any given point within the flow, the gas is illuminated by light from a central point source. This simplified approach is not a problem unless the wind is located at distances very close to the black hole ($\leq 100r_{\rm g}$). The SEDs for this radiation have been discussed in the previous Sect. 3.1.

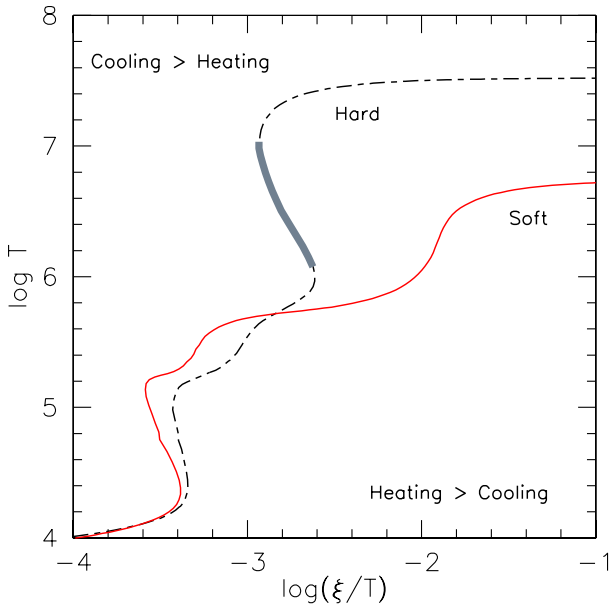

Fig. 3. Stability curves for photoionized gas with Solar abundance, $n_{\rm H} = 10^{10}$ cm^{-3} and $N_{\rm H} = 10^{23}$ cm^{-2} being illuminated by the Soft and the Hard SEDs. A part of the Hard stability curve is highlighted in thick grey; this is the negative slope part of the curve and corresponds to unstable thermodynamic equilibrium. Gas with $\log\xi$ in this part of the curve is unlikely to exist in nature. The Soft curve is stable in the relevant part ($\log T \geq 5.5$). We note that both curves have a part with negative slope at $\log T \lesssim 5.0$. However, this part of the stability curve has very low values of $\log\xi$ (<2.0), which are not relevant for gas around BHBs.

To detect the presence of ionized gas, we need to evaluate if the ionization parameter of the gas is thermodynamically stable. Any stable photoionized gas will lie on the thermal equilibrium curve or stability curve of $\log T$ versus $\log(\xi/T)$ (Fig. 3). This curve is often used to understand the structure of absorbing gas in AGN (Chakravorty et al. 2008, 2009a,b, and references therein) and BHBs (Chakravorty et al. 2013; Higginbottom & Proga 2015). If the gas is located (in the $\xi - T$ space) on a part of the curve with negative slope then the system is considered thermodynamically unstable because any perturbation (in temperature and pressure) would lead to runaway heating or cooling. Gas lying on the part of the curve with positive slope, on the other hand, is thermodynamically stable to perturbations and hence likely to be detected when they cause absorption lines in the spectrum.

With version C08.00 of CLOUDY[3] (Ferland et al. 1998) we generated stability curves using both the Soft and the Hard SEDs as the ionizing continuum. For the simulation of these curves we assumed the gas to have solar metallicity, $n_{\rm H} = 10^{10}$ cm^{-3} and $N_{\rm H} = 10^{23}$ cm^{-2}. Assuming these representative average values of $n_{\rm H}$ and $N_{\rm H}$ are reasonable because the stability curves remain invariant when these two parameters are varied over a wide range spanning several decades (see Chakravorty et al. 2013, for

[3] URL: http://www.nublado.org/

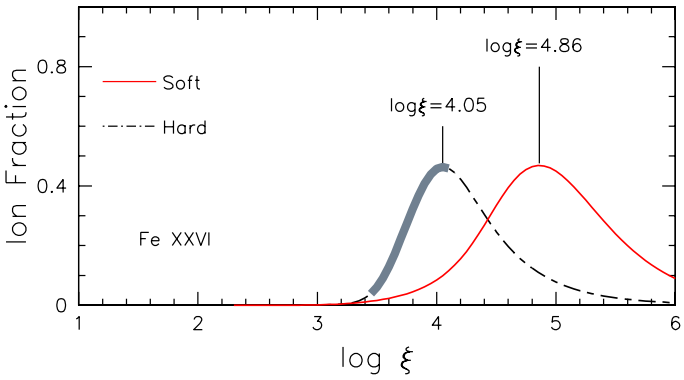

Fig. 4. Ion fraction distribution of FeXXVI with respect to $\log\xi$ is shown for the two SEDs, Soft and Hard. The peak of the distribution is marked and the corresponding $\log\xi$ values are labelled. We note that for the Hard SED, a part of the distribution is highlighted by thick grey line, which corresponds to the thermodynamically unstable range of ξ.

details). The Soft stability curve (solid red line in Fig. 3) has no unstable region, whereas the Hard curve (dot-dashed black line) has a distinct region of thermodynamic instability (thick grey line). This part of the curve corresponds to $3.4 < \log\xi < 4.1$. Thus, this range of ionization parameter has to be considered undetectable when we are using the Hard SED as the source of ionizing light.

A survey of the literature shows that it is usually absorption lines from H- and He-like Fe ions that are detected (e.g. Lee et al. 2002; Neilsen & Lee 2009; Miller et al. 2004, 2006; and King et al. 2012). In fact, it is the absorption line from FeXXVI that is most often observed. A very important compilation of detected winds in BHBs was presented in Ponti et al. (2012), and this paper also concentrates the discussion around the line from FeXXVI. Hence, we choose the presence of the ion FeXXVI as a proxy for detectable winds. The probability of the presence of an ion is measured by its ion fraction. The ion fraction $I(X^{+i})$ of the X^{+i} ion is the fraction of the total number of atoms of the element X that are in the ith state of ionization. Thus,

$$I(X^{+i}) = \frac{N(X^{+i})}{f(X)\,N_{\rm H}},$$

where $N(X^{+i})$ is the column density of the X^{+i} ion and $f(X) = n(X)/n_{\rm H}$ is the ratio of the number density of the element X to that of hydrogen. Figure 4 shows the ion fraction of FeXXVI calculated using CLOUDY. The ion fractions are, of course, different based on whether the Soft or the Hard SED has been used as the source of ionization for the absorbing gas. The value of $\log\xi$, where the presence of FeXXVI is maximized, changes from 4.05 for the Hard state, by ~0.8 dex, to 4.86 for the Soft state.

In the light of all the above mentioned observational constraints, we will impose the following physical constraints on the MHD outflows (in Sects. 4 and 5) to locate the detectable wind region within them:

- in order to be defined as an outflow, the material needs to have positive velocity along the vertical axis ($z_{\rm cyl}$);
- over-ionized gas cannot cause any absorption and hence cannot be detected. Thus, to be observable via FeXXVI absorption lines we constrain the material to have an upper limit for its ionization parameter. We imposed that $\xi \leq 10^{4.86}$ erg cm (peak of FeXXVI ion fraction) for the Soft state. The ion fraction of FeXXVI peaks at $\xi = 10^{4.05}$ for the Hard state, but this value is within the thermodynamically unstable range. Hence, for the Hard state, the constraint is $\xi \leq 10^{3.4}$ erg cm, the value below which the thermal equilibrium curve is stable;
- the wind cannot be Compton thick and so we impose that the integrated column density along the line of sight satisfies $N_{\rm H} < 10^{24}$ cm^{-2}.

3.3. Finding the detectable wind within the MHD outflow

In this section we demonstrate how we choose which part of the MHD outflow will be detectable through absorption lines of FeXXVI. For the demonstration we use the MHD solution with $\varepsilon = 0.001$ and $p = 0.04$, which is illuminated by the Soft SED. Hereafter we refer to this set of parameters as the "Best Cold Set". For the purpose of discussion in this section, we work with the Soft SED only, but in subsequent sections additional calculations are carried out for the scenario where the MHD outflow is illuminated by the Hard SED.

The Best Cold MHD solution provides us with the knowledge of the density of the material at each point within the outflow. Furthermore, we know the Soft SED (both shape and intensity) and so at each point in the outflow we can calculate the ionization parameter $\xi = L_{\rm ion}/(n_{\rm H}R^2_{\rm sph})$. Figure 5 shows the ionization parameter distribution (colour gradient) and the density distribution (iso-density contours on the lower panel) of the outflow due to the Best Cold Set. The solid black lines threading through the distribution shows the magnetic field lines along which material is outflowing. The MHD solutions are mathematically self-similar in nature, which essentially means that we can propagate the solutions infinitely. However, we have restricted the last streamline to be anchored at $r_{\rm o} = 10^7 r_{\rm g}$. The top panel of the figure is a complete view, which shows the entire span of the MHD solution that has been evaluated.

To find the wind region (detectable through FeXXVI absorption lines) within this outflow we have to impose the three required physical conditions listed in Sect. 3.2. The resultant wind region is highlighted as the yellow wedge in Fig. 5. We see that the wind is detected only from the outer parts of the flow with $\log R_{\rm sph}|_{\rm wind}/r_{\rm g} \geq 5.4$. The lowest and highest equatorial angle (i) of the line of sight are clearly marked for the wind region (in both panels). The observer will have to view the BHB within this angular range to be able to detect the wind. The wind is equatorial, for the Best Cold Set, not extending beyond $i = 26.9°$. In the lower panel of Fig. 5 we use a linear scale (but normalized by $10^7 r_{\rm g}$) for $r_{\rm cyl}$ and $z_{\rm cyl}$, which gives us a close-up view of the wind region within the solution. The labelled dashed lines are the iso-contours for the number density $\log n_{\rm H}({\rm cm}^{-3})$. The velocities $v_{\rm obs}$ (not shown in the figure) in this region fall within the range 10–100 km s^{-1}.

This same method of finding the wind and the associated physical conditions is used for all the cold MHD solutions considered in this paper. In the subsequent sections we will vary the MHD solutions (i.e. ε and p) and investigate the results using both the Soft and Hard SEDs.

To ensure that the wind is in thermal equilibrium, it is important to compare the various physical timescales. We used CLOUDY to evaluate the cooling timescales at each point within the wind region of the solution. CLOUDY assumes that atomic processes (including photoionization and recombination cooling) occur on timescales that are much shorter than other changes in the system, so that atomic rates have had time to become "time-steady". These atomic processes, in addition to some other continuum processes like Comptonization

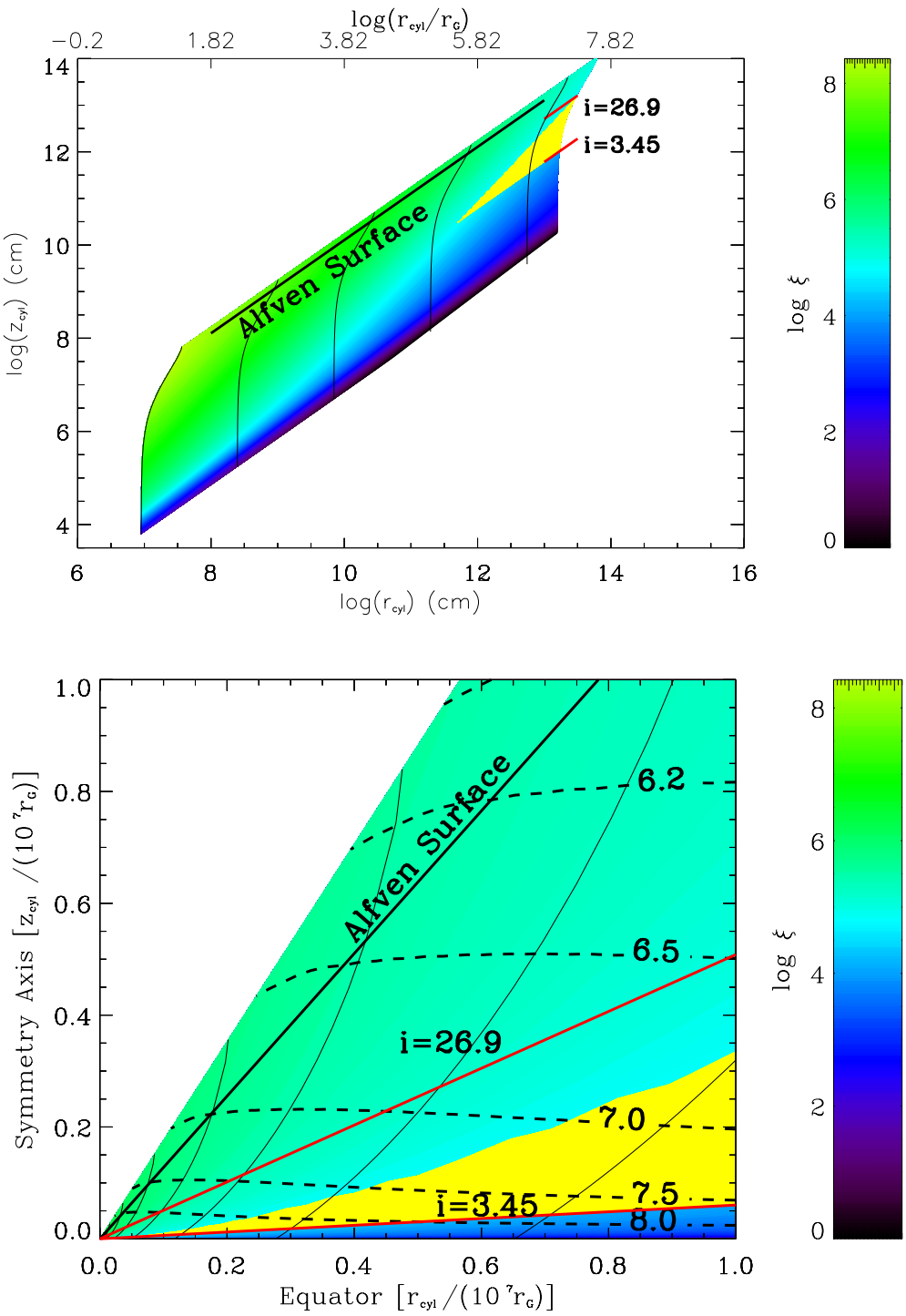

Fig. 5. *Top panel*: distribution of the Best Cold Set in the logarithmic plane of the radial ($r_{\rm cyl}$) and vertical ($z_{\rm cyl}$) distance (in cylindrical co-ordinates) from the black hole. The distances are also expressed in terms of the gravitational radius $r_{\rm g}$ (*top axis*), which is 1.5×10^6 cm for a 10 $M_\odot$ black hole. The colour gradient indicates the ξ distribution of the flow. The solid black lines threading through the distribution show some of the magnetic field lines along which material is outflowing. The Alfvén surface corresponding to the solution is also marked and labelled. The yellow wedge highlights the wind part of the flow; this material is optically thin with $N_{\rm H} < 10^{24}$ cm^{-3} and has sufficiently low ionization parameter (with $\xi < 10^{4.86}$ erg cm) to cause FeXXVI absorption lines. The angular extent of the wind is also clearly marked, where i is the equatorial angle. *Bottom panel*: a close-up view of the wind region. The distances are expressed in linear scale, but normalized to $10^7 r_{\rm g}$. The dashed lines show the isocontours of $n_{\rm H}$, while the associated labels denote the value of $\log n_{\rm H}$ (cm^{-3}).

and bremsstrahlung, are responsible for heating and cooling the gas. Whether the atomic processes dominate over the continuum processes is determined by the ionization state and/or the temperature of the gas. For photoionized wind we expect the atomic processes to dominate. However, one way to make sure that the gas satisfies the time-steady condition (which is assumed by CLOUDY) is to check the CLOUDY computed cooling timescale against the dynamical timescales from our physical MHD models. CLOUDY defines the cooling timescale as the time needed to lose half of the heat generated in the gas via

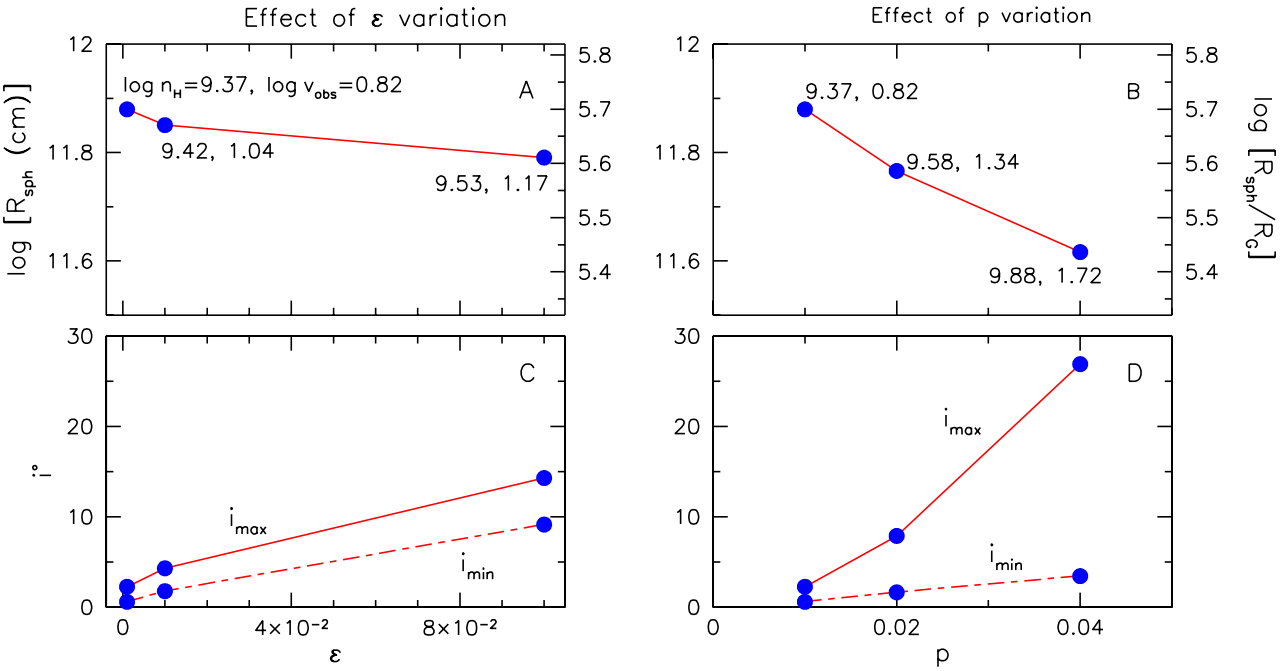

Fig. 6. Physical parameters of the wind are plotted as a function of ε (*left panels*) and p (*right panels*), while using the Soft SED as the ionizing continua. *Top panels*: for the closest wind point, we plot the logarithm of $R_{\rm sph}|_{\rm wind}$ in the *left panel* A as a function of the disk aspect ratio ε and as a function of the accretion index p in the *right panel* B. This index is held constant at $p = 0.01$ for the solutions in the *left panels* and $\varepsilon = 0.001$ is kept constant for those in the *right panels*. Each blue circle in the figure represents a MHD solution. The logarithm of two other relevant quantities, $n_{\rm H}$ and $v_{\rm obs}$ for the closest wind point, are labelled at each point; these are their maximum possible values within the wind region for a given MHD solution. *Bottom panels*: the minimum ($i_{\rm min}$) and the maximum ($i_{\rm max}$) equatorial angles of the line of sight, within which the wind can be observed, is plotted as a function of ε (*left*) and of p (*right*).

various atomic and continuum processes. Thus, thermal equilibrium is also ensured as long as the cooling timescale is smaller than the dynamical timescale $\tau_{\rm dyn}$, which was found to be true within the wind region of the outflow for the Best Cold Set.

4. Cold MHD solutions

4.1. Effect of variation of the parameters of the MHD flow

Here we aim to find which of the two parameters ε and p is more influential in producing the wind. The value of p and ε decides the density of material at the launching point of our magneto-hydrodynamic outflow (Eq. (2)). The extent of magnetization in the outflow is also dependant on p (Sect. 2). It is these two parameters that link the density and other physical properties of the outflow with the accretion disk. Since a particular pair of p and ε will result in a unique MHD solution, we can generate different MHD solutions by changing the values of p and ε. We perform the methods described in the previous Sect. 3.3 on each of these solutions, and investigate the wind part of the outflow.

To judge the influence of p and ε in a quantitative way, we compare some physically relevant parameters of the wind. For observers, one important set of wind parameters are the distance, density, and velocity of the point of the wind closest to the black hole. Hereafter we call this point the "closest wind point". Another quantity of interest would be the predicted minimum and maximum angles of the line of sight within which the wind can be observed. We conduct this exercise using both the SEDs, Soft and Hard. The results are plotted in Fig. 6.

The exact value of these quantities should not be considered very rigorously because the value is decided by the various constraints that we have applied. It is more important to note the changes in these quantities as ε and p vary. The relative changes should be used to assess how variations in ε and p increase the possibilities of detecting the wind.

4.1.1. Variation of the disk aspect ratio ε

For the closest wind point, we plot $R_{\rm sph}|_{\rm wind}$ versus the value of ε of the MHD solution (panel A of Fig. 6); $n_{\rm H}$ and $v_{\rm obs}$ are also labelled. Using the Soft SED, the closest wind point reaches closer to the black hole by a factor of 1.06 as ε increases from 0.001 to 0.01, and then by a farther factor of 1.14 as ε increases to 0.1. The density at the closest point is $n_{\rm H}|_{\rm max} = 10^{9.37}{\rm cm}^{-3}$ for $\varepsilon = 0.001$. We note that for any given solution, the density at the closest point is the maximum attainable density within the wind region for that particular MHD solution. This maximum attainable density of the wind increases as ε increases to 0.01 and then to 0.1. However, as a function of ε, the variation in this quantity is not very high, only 0.16 dex. Like density, for a given solution the velocity at the closest wind point, $v_{\rm obs}|_{\rm max}$, is the highest that can be attained by the detectable wind. This quantity monotonically decreases by 0.22 dex and then by 0.13 dex as ε increases from 0.001 to 0.01 and then to 0.1. This means, to get winds with higher speed, we need disks with higher aspect ratios.

The parameters $i_{\rm min}$ and $i_{\rm max}$ are the minimum and maximum equatorial angles of the line of sight within which the wind can be detected. Panel C of Fig. 6 shows the changes in the angles as ε varies. The angular extent of the wind can be easily judged by gauging the difference between $i_{\rm min}$ and the maximum angles for a particular solution (and SED). As ε varies from 0.001 to 0.01 to 0.1, $i_{\rm min}$ rises from 0.60 to 1.78 to 9.15 and $i_{\rm max}|$Soft increases from 2.27 to 4.31 to 14.3. The growth of $\Delta i = i_{\rm max} - i_{\rm min}$ with ε shows that the wind gets broader as the disk aspect ratio increases.

4.1.2. Variation of the ejection index p

As p increases, the wind moves closer to the black hole (panel B of Fig. 6); $R_{\rm sph}|_{\rm wind}$ drops by a factor of 1.3 as p goes from 0.01 to 0.02 and then reduces further by a factor of 1.41 when p is increased to 0.04 while using the Soft SED. The total change in the density of the closest wind point is 0.51 dex as p changes from 0.01 to 0.04. Thus, both $R_{\rm sph}|_{\rm wind}$ and $n_{\rm H}|_{\rm max}$ are affected more by the variation in p than by the variation in ε (within the range of these parameters that we investigated). Similarly, the velocity $v_{\rm obs}|_{\rm max}$ of the closest point varies more with change in p: the total increase is 0.9 dex.

In panel D of Fig. 6, $i_{\rm min}$ and $i_{\rm max}$ is shown as a function of p (using the Soft SED). As p goes from 0.01 through 0.02 to 0.04, the minimum angle rises from 0.60 through 1.65 to 3.45, a range much smaller than that caused by the ε variation. Instead, $i_{\rm max}$ goes from 2.27 to 7.89 to 26.9. Thus the growth of Δi is rendered higher as a function of increase in p, implying a higher probability of detecting a wind when the flow corresponds to higher p values. Since p is the relatively more dominant disk parameter (compared to ε) in increasing the density at a given distance, the resultant outflowing material has lower ionization. This is a favourable influence on detectable winds.

4.2. Cold solutions for the Hard state

For the entire range of ε (0.001–0.1) and p (0.01–0.04) we also analysed the MHD solutions illuminated by the Hard SED. We note that for the Hard SED we have to modify the upper limit of ξ according to the atomic physics and thermodynamic instability considerations (Sect. 3.2). With the appropriate condition, $\log \xi \leq 3.4$, we could not find any wind portions within the Compton thin part of the outflow for any of the MHD solutions.

This is a very significant result because it provides strong support to the observations that BHBs do not have winds in the Hard state. We discuss this issue further and include better quantitative details in Sect. 6.3.

4.3. The need for Warm MHD solutions

The density reported for most of the observed BHB winds $\geq 10^{11}$ cm^{-3} and the distance estimates place the winds at $\leq 10^{10}$ cm (Schulz & Brandt 2002; Ueda et al. 2004; Kubota et al. 2007; Miller et al. 2008; Kallman et al. 2009). Our analysis in the previous sections shows that $R_{\rm sph}|_{\rm wind}$ is too high and $n_{\rm H}|_{\rm max}$ is too low even for the Best Cold Solution to match observations. The purpose of this section is to understand which parameter of the accretion-ejection process can provide us with a MHD solution capable of explaining observed (or derived) parameters of BHB winds. Studying the effect of the disk parameters gives us a clear indication that increasing the value of the ejection index p favours the probability of detecting winds, as demonstrated by the larger extent of increase in Δi. Furthermore, the increase in p results in two more favourable effects: the closest wind point moves closer to the black hole and causes a higher increase in density.

The above phenomenological tests of the $\varepsilon - p$ space indicate that a MHD solution with higher ε (e.g. 0.01) and a high $p \geq 0.04$ would be the best choice to produce detectable winds, comparable to observations. However, there are limitations on the $\varepsilon - p$ combination imposed by the physics of the MHD solutions (see Fig. 1) and it is not possible to reach higher values of p for the cold solutions with isothermal magnetic surfaces. As shown in Casse & Ferreira (2000b), to get denser outflows with higher p, some additional heating needs to take place at the disk upper layers leading to a warming up of the wind. The authors argued that the origin of this extra heating could be the illumination from an external source or enhanced turbulent dissipation within the disk surface layers. In the following section we investigate whether a warm solution is indeed much better for producing winds that match observations.

5. Warm MHD solutions

In this section we investigate the properties of the wind as a function of increasing p, but for warm MHD solutions. Here we choose to ignore the effect of ε because in the previous section we found that variation in ε (over two orders of magnitude) has very little effect on the physical quantities of the wind. Furthermore, in the previous sections we find that the wind does not exist for the Hard SED. Hence, we conduct the extensive calculations with the Soft SED only. However, we discuss winds in the Hard state in Sect. 6.3 as a part of the general discussions.

Self-confined outflows require $\sigma^+ \simeq 1/p$ larger than unity, as pointed out through Eq. (4) in Sect. 2.2. Moreover, the power in the outflow is always a sizable fraction of the mechanical power

$$L_{\rm acc} = \left[\frac{GM_{\rm BH}\dot{M}_{\rm acc}(r)}{2r}\right]_{r_{\rm out}}^{r_{\rm in}} \tag{13}$$

released by the accreting material between the inner radius $r_{\rm in}$ and the outer radius $r_{\rm out}$. Because $\dot{M}_{\rm acc}(r) \propto r^p$ in a disk, $L_{\rm acc} = 0$ is obtained for $p = 1$, which is why, unless there is an external source of energy, $p = 1$ is a maximum limit; in fact, powerful magnetically driven flows require a much smaller ejection index. To consider what highest value of p should be aimed for, we scouted the literature and found two relevant references:

(a) Casse & Ferreira (2000b) who computed warm MHD accretion-ejection solutions up to $p = 0.456$ to model winds mostly, in young stellar objects; and
(b) a series of papers by Fukumura et al. (Fukumura et al. 2010a,b, 2014, 2015), who used a model with $p = 0.5$.

Therefore, while attempting to generate the disk surface heated, magnetically driven, and magnetically confined outflows, we limit ourselves to $p \leq 0.5$.

For this paper, we obtain dense warm solutions (with higher values of p, i.e. $p \geq 0.04$) through the use of an ad hoc heating function acting along the flow. This additional heating needs to start within the disk itself, in the resistive MHD layers, in order to cause a larger mass loading at the base of the outflow. However, the heating must be maintained for some distance within the outflow too, into the ideal MHD zone. This is necessary in order to help the launching of these dense outflows and to tap the thermal energy content instead of the magnetic content (refer to Casse & Ferreira 2000b, for more details). It must therefore be realized that any given "warm solution" from a near Keplerian accretion disk is based on an ad hoc heating term (the function Q in Casse & Ferreira 2000b, see also Appendix A). The physical mechanism behind the heating term has not been specified. However, a posteriori calculations show that even a small percent of the released accretion energy would be enough to give rise to such warm MHD winds. Whether or not MHD turbulence in accretion disks can provide such surface heating is an open theoretical issue. For further discussion on this, see Appendix A. On the other hand, the heating could be caused by the illumination from the interior parts of the disk. To determine and/or distinguish between the physical causes of the heating is a rigorous theoretical study in itself and is beyond the scope of this paper.

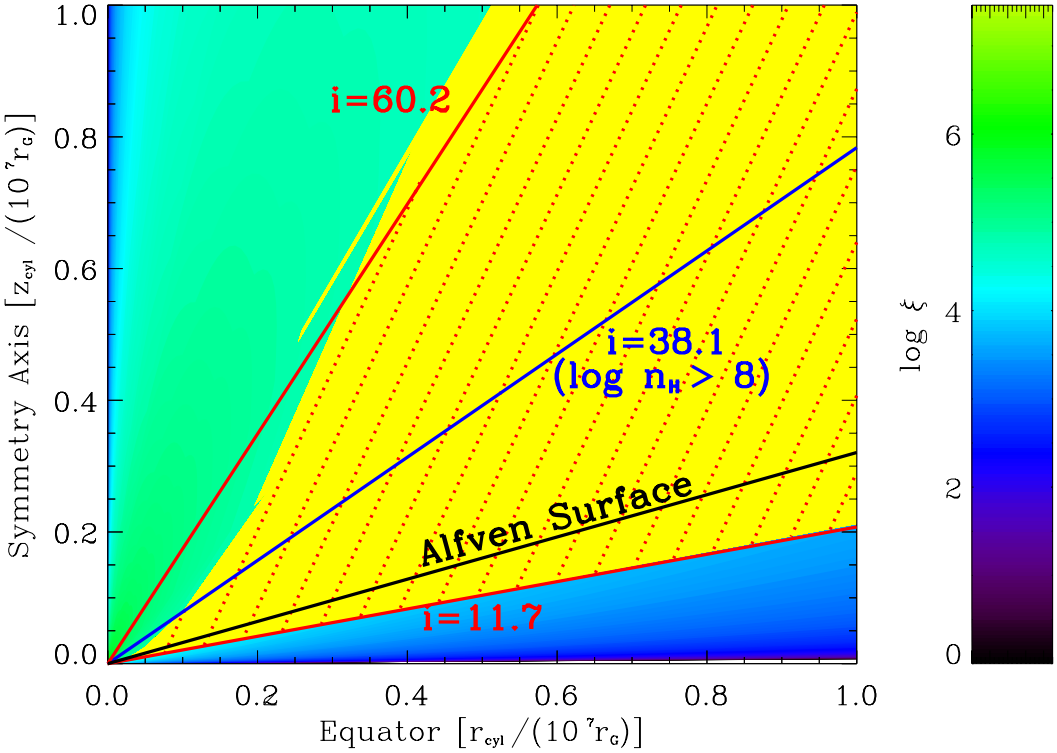

Fig. 7. Ionization parameter distribution for a Warm MHD solution with $\varepsilon = 0.01$ and $p = 0.10$. The yellow region within the outflow is obtained in the same way as in Fig. 5. The shaded region (with dotted red lines) is the wind region within such a warm outflow; to obtain this region we used the additional constraint that the cooling timescale of the gas has to be lower than the dynamical timescale. Furthermore, the solid blue line with $i = 38.1°$ is drawn to depict that high density material ($\log n_{\rm H} \geq 8.0$) in the flow is confined to low equatorial angles.

To ease comparison between various warm models, we use the same shape for the heating function, while playing only with its normalization to increase p (the larger the heat input, the larger the value of p, see Fig. 2 in Casse & Ferreira 2000b). For $\varepsilon = 0.01$ we could achieve a maximum value of $p = 0.11$. For the purpose of this paper, providing the "most massive" (i.e. largest possible $p = 0.5$) solution is not required; it is enough to show general trends. However, we are developing the methods to generate denser MHD solutions with $p = 0.5$ and these solution(s) will be reported in our subsequent publications where we will attempt to model the winds observed in specific outbursts of specific BHBs.

Figure 7 shows the wind for a Warm MHD solution with a rather high $p = 0.10$. The wind (yellow region) spans a much wider range than even the Best Cold Solution and extends far beyond the Alfvén surface, which was not the case for the cold MHD solutions. Hence, we introduce an additional constraint derived from timescale considerations. The lower angular limit ($i = 11.7°$) is derived from the constraints of ξ and $N_{\rm H}$. Next, we used CLOUDY to calculate the cooling timescales of the gas at each point within the yellow wind region of the outflow. We note that for the timescale calculations using CLOUDY (which are computationally expensive) we used a much coarser grid of i than that used for other calculations of the MHD solutions; a coarse upper limit on i is sufficient for our purposes here. To be consistent with a photoionized wind, which is in thermal equilibrium, the cooling timescale needs to be shorter than the dynamical timescale. This timescale condition was satisfied within the yellow region if $i \leq 60°$. Thus the red-dotted shaded region is the resultant detectable wind. However, we note that the densest part of the wind is confined to low equatorial angles. For example, gas with $n_{\rm H} \geq 10^8$ cm^{-3} will lie below $i = 38.1°$. For this solution, we further calculated $B_z \sim 70$ Gauss (Eq. (6)) at the disk mid-plane at a distance $r_{\rm cyl} = R_{\rm sph} = 1.28 \times 10^{11}$ cm.

We investigated warm MHD solutions with a range of values of p. In Fig. 8 we have plotted the distance of the closest wind point for all these solutions. Each point is also labelled with the respective values of density and velocity. Between the $p = 0.04$ solution and the one with the highest $p = 0.11$ (that we could achieve) $R_{\rm sph}|_{\rm wind}$ goes closer by a factor of 3.79 and stands at $7.05 \times 10^4\, r_{\rm g}$. The highest density that we could achieve is $\log n_{\rm H} = 11.1$ and the highest velocity is $\log v_{\rm obs} = 2.92$. Hereafter we refer to the $\varepsilon = 0.01$ and $p = 0.10$ warm MHD solution as the "Best Warm Solution".

Clearly, warm solutions do a much better job than cold ones, as expected. However, some observational results require the winds to have higher density and lower distance than those produced by the Best Warm Solution. In the following section we discuss how we can theoretically achieve the more stringent values demanded by the observations of some extreme winds.

6. Discussions

6.1. Towards the extreme MHD winds

6.1.1. Choice of upper limit of ξ

The ionization parameter is the key parameter in defining the wind region within the outflow. Here we discuss (a) the possibility of changing ξ if $\dot{m}$ changes; and (b) the effect if the upper limit of ξ is changed.

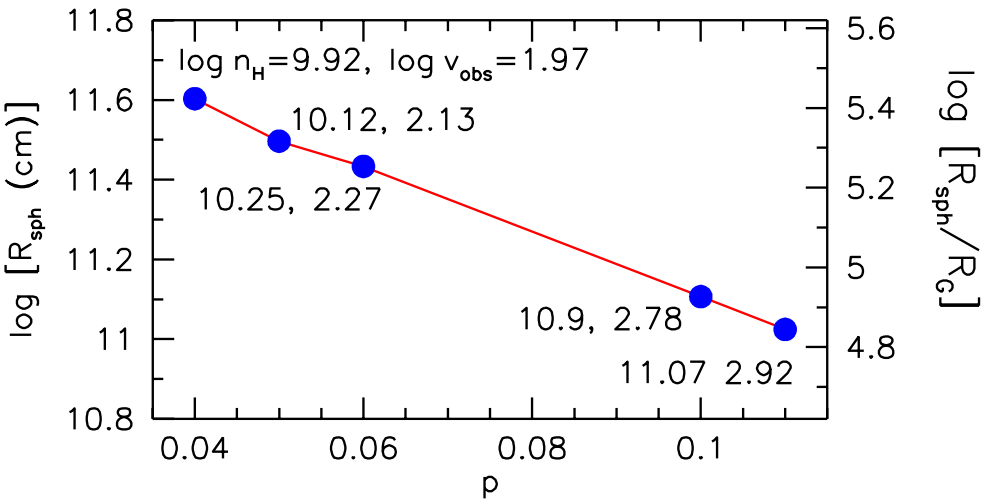

Fig. 8. Distance of the closest wind point is plotted as a function of p for all the warm MHD solutions that we investigated. Density and velocity are also labelled. $\varepsilon = 0.01$ is constant.

(a) In the definition of ξ, the density $n_{\rm H}$ in the denominator is proportional to $\dot{m}$ (see Eq. (6)). In the numerator, $L_{\rm ion} \propto L_{\rm rad}$ and we also assume $L_{\rm rad}$ to be proportional to $\dot{m}$ (see Sect. 3.1). Hence, for a given MHD solution, changing $\dot{m}$ will not change the ξ distribution within the outflow.
In the case of inefficient accretion flow like ADAF, $L_{\rm rad} \propto \dot{m}^2$ and changes in $\dot{m}$ could have some effects. However, we are considering physical scenarios here, where the accretion disk is radiatively efficient with $\dot{m}_{\rm obs} \sim 0.1$. Hence, accepting $L_{\rm rad} \propto \dot{m}$ is a reasonable assumption.

(b) We used the limit $\log \xi \leq 4.86$ to define the detectable wind. We note that for the Soft SED, $\log \xi = 4.86$ corresponds to the peak of the ion fraction of FeXXVI (Fig. 4). The ion can have a significant presence at higher ξ. For example, at $\log \xi = 6.0$ FeXXVI is still present, but at ~1/4 of its peak value. Furthermore, there are other ions (including NiXXVIII) that peak at higher values of ξ (see Fig. 4 of Chakravorty et al. 2013). These ions have been reported in Miller et al. (2008). In fact they may be routinely detected in data from the future X-ray telescopes like Astro-H and Athena. It is thus instructive to investigate how the properties of the closest wind point (for a given solution) are modified when the constraints on the upper limit of $\log \xi$ are changed.

For the best warm solution we calculated the physical parameters for the closest wind point with a modified upper limit $\log \xi = 6.0$. We find that $R_{\rm sph}|_{\rm wind}$ decreases by a factor of 93.4 bringing this point to $9.1 \times 10^2 r_{\rm g}$. The density at this point is $\log n_{\rm H} = 13.71$ and the velocity is $\log v_{\rm obs} = 3.71$. Thus, we see that the parameters of the closest point is sensitively dependant on the choice of the upper limit of ξ.

6.1.2. Denser warm solutions

From the analysis presented in Sects. 4.1 and 5 it is clear that MHD solutions with larger p favour winds that are closer to the black hole. Even for the densest solution discussed in this paper, with $\varepsilon = 0.01$ and $p = 0.11$, we cannot predict a wind closer than $7.05 \times 10^4\ r_{\rm g}$ (for $\log \xi \leq 4.86$) and denser than $\log n_{\rm H} > 11.07$. However, Miller et al. (2008) discussed that the wind in GRO J1655-40 was very dense, where $\log n_{\rm H} \geq 12$, and so had to be very close to the black hole at $\sim 10^3 r_{\rm g}$. Thus, to explain such extreme winds, we need denser warm MHD solutions with higher p.

In the context of AGN, Fukumura et al. (2010a,b, 2014, 2015) have been able to reproduce the various components of the absorbing gas using MHD outflows that would correspond to $p \simeq 0.5$. As discussed in Sect. 5, we have not been able to reproduce such high values of p and are limited to $p = 0.11$. Our calculations in the previous section shows that as p increases from 0.04 to 0.11 for the warm MHD solution, $R_{\rm sph}|_{\rm wind}$ for the closest wind point decreases by a factor of 3.79. Thus a further increase to $p \simeq 0.5$ may take the closest wind point nearer to the black hole by a further factor of ~10 to $\sim 5 \times 10^3 r_{\rm g}$. The above hypothetical numbers assume an almost linear change in density as p increases. In reality, the progression of the physical quantities in the denser MHD solutions may not be that simple. We shall report the exact calculations in our future publications.

As our analyses stand now, even with denser warm MHD solutions with $p = 0.5$ we do not expect the wind to exist closer than $\sim 5 \times 10^3 r_{\rm g}$ if $\log \xi < 4.86$. However, as we discuss in the previous subsection, this distance may be reduced by a factor of ~90 to few $< 10^2 r_{\rm g}$ for a modified constraint of $\log \xi < 6.0$; the density and velocity increase accordingly. These speculative numbers indicate that indeed the warm MHD outflow models may be able to explain even the most extreme winds observed (Miller et al. 2008; King et al. 2012; Diaz Trigo et al. 2013). The above speculations strongly indicate to us the kind of MHD solutions that we need to generate to fit observations. However, a confirmation of these speculations is beyond the scope of this paper. We will report the exact calculations for the extreme MHD models in our subsequent papers.

6.2. Temperature of the outflowing gas

The physical properties of the MHD solutions depend on the energy equation, which involves solving the balance between the local heating and cooling effects. Hence, along with all the other properties, such as the velocity and density, the temperature ($T_{\rm MHD}$) of the outflowing gas is also specified (see discussion in Appendix A). However, the MHD calculations do not take into account the effect of photoionization of the outflowing material due to light from the central source. In fact, the temperature of the gas within the wind region is determined by

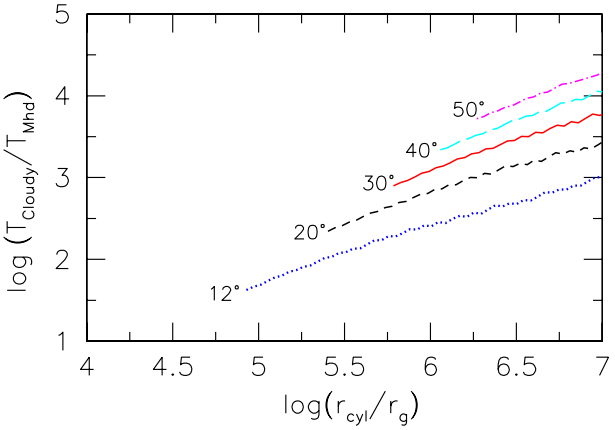

Fig. 9. Comparison of the different temperatures associated with wind in the Best Cold Solution. $T_{\rm Cloudy}$ is the temperature calculated using CLOUDY and is the actual temperature of the photoionized gas. $T_{\rm MHD}$ is the temperature due to the MHD solution, the value that has been used to calculate all the physical properties of the outflow. The ratio between these two temperatures is plotted as a function of the distance from the black hole and at different angles of line of sight.

the effects of photoionization by the ionizing SED and may be very different from $T_{\rm MHD}$.

We used CLOUDY to calculate the temperature $T_{\rm Cloudy}$ of the gas to check how different it is from $T_{\rm MHD}$ for the best warm solution and the comparison is shown in Fig. 9. CLOUDY calculations are computationally expensive and so we restricted them to within the wind region (the shaded region with dotted red lines) of the outflow alone. We note that for the best warm solution, below $i = 11.7°$ the gas is Compton thick with integrated $N_{\rm H} > 10^{24}$ cm^{-2}. Hence photoionization and associated acceleration of the Compton thick gas may be negligible. As such, the properties of the outflow in the Compton thick region of the outflow is likely to be determined by magnetic fields alone. To determine whether this qualitative assumption is true is beyond the scope of the paper (although, see Sect. 3.4 of Garcia et al. 2001 for detailed methodology of how one might attempt to solve the energy equation along a flow field line involving both the MHD dynamical terms and a photoionization code). Hence we compare temperatures within the Compton thin wind region only.

Figure 9 shows that $T_{\rm Cloudy}$ is indeed different from $T_{\rm MHD}$ and the difference increases as we move away from the surface of the accretion disk and as we move further out. We need to judge at this point whether this difference in the gas temperature, and hence on its enthalpy, makes a difference to the properties of the gas.

Figures A.3 and A.4 show that the specific enthalpy term is negligible compared to the specific magnetic energy. Comparing the specific energies, we see that even if the gas temperatures were higher (due to photoionization) than $T_{\rm MHD}$ by orders of magnitude, the magnetic field would still dominate the specific energy and hence the properties of the outflow would still be determined by the magnetic field.

6.3. Effect of thermodynamic instability in the Hard state

Conventionally it is assumed that ionized gas cannot be detected if it is thermodynamically unstable. Chakravorty et al. (2013) showed the effect of thermodynamic considerations and found the equilibrium curve to be unstable for a range of ξ values, but only for the Hard SED. We conducted a stability curve analysis in Sect. 3.2 and find similar results for the Hard SED: the range $3.4 < \log\xi < 4.1$ is thermodynamically unstable. Thus, the constraints on ξ have to be modified accordingly when looking for the wind region within an outflow illuminated by the Hard SED.

In Sect. 4.2 we mention that with the appropriate restrictions on the ξ value, no wind could be found within the cold MHD outflows. Since the warm solutions result in much broader wind regions than the cold solutions do, we test whether the best warm solution can have a wind with a Hard SED.

Using the value $\log\xi = 4.05$, we get a significant wind region (although lower than the Soft SED case). Next, we check the effect of thermodynamic instability. In Fig. 10 the pink region shows the part of the outflow that has $\log\xi = 3.4$–4.05, a range that is thermodynamically unstable. We note that above the $i = 11.9°$ line (which marks the Compton thick limit), this thermodynamically unstable zone almost completely occults the wind region (in yellow). This implies that in the Hard state, even if a significant region of the outflow is Compton thin and has the correct $\log\xi$ to produce FeXXVI lines, this same region is also thermodynamically unstable. Hence in the Hard state, we cannot expect to detect the wind.

Our analysis thus strongly suggests that winds will not be detected in the Hard state. Hence, we are in agreement with observational results which detect winds only in the Softer states of the outburst (Ponti et al. 2012). We note that such a correlation between accretion state (Softer) and the presence of wind has also been found for neutron stars by Ponti et al. (2014). Thus our analysis and results may be valid, not only for BHBs but for neutron star accretion disks as well.

Here we want to discuss an interesting observation made by Higginbottom & Proga (2015) on the issue of thermodynamic instability. The authors correctly point out that if a parcel of gas reaches a thermodynamically unstable temperature (where the gradient of the stability curve becomes negative; see Fig. 3) the gas will quickly heat up to attain the higher temperature of the next thermodynamically stable point at the same pressure (the same ξ/T). For a thermally driven wind this effect would result in very efficient acceleration. However, for a MHD wind this effect, particularly relevant for the Hard State, will not aid in the wind driving mechanism. In the Hard state (from Fig. 3) the maximum increase in temperature for a parcel of gas to avoid thermodynamic instability is about an order of magnitude. In the previous subsection we demonstrated that $T_{\rm Cloudy}$ could be much higher than $T_{\rm MHD}$ and still not affect the properties of the MHD driven wind. For a typical angle of $i = 20°$ (see Figs. 9 and A.4), even if $T_{\rm Cloudy}$ were higher by an order of magnitude (raised by thermodynamic instability considerations), the magnetic specific energy would still dominate over that of enthalpy. Hence, for MHD winds, thermodynamic instability is unlikely to cause any additional efficient acceleration. We acknowledge that thermal lifting might play a role in the disk upper layers where the disk material is magneto-centrifugally accelerated, but it is unclear whether or not photoionization equilibrium would correctly describe these highly expanding layers.

7. Conclusions

Winds are detected as absorption lines in the high resolution X-ray spectra of black hole binaries. The absorption lines are mostly from H-like and He-like Fe, but some rare observations show lines from other ions. Ponti et al. (2012) have shown that winds are seen in the Soft state of the outburst and never in the canonical Hard states. Furthermore, the strongest winds were observed for objects with high inclination angles, i.e. the

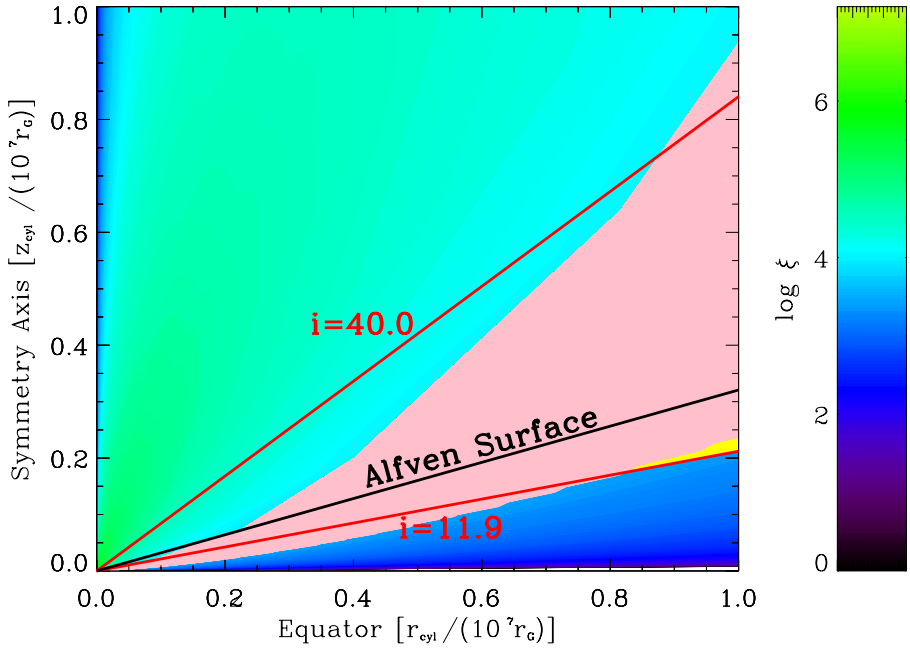

Fig. 10. Wind characteristics when the Best Warm Solution is illuminated with a Hard SED. The drastically reduced yellow region within the outflow (cf. Fig. 7) is obtained in the same way as in Figs. 5 and 7. We can only see a very small portion of this yellow region at $r_{\rm cyl}/(10^7 r_{\rm g}) > 0.8$. The rest of this yellow region is occulted by the pink wedge, which represents the thermodynamically unstable part of the outflow that has $3.4 \leq \log \xi \leq 4.05$. We note that a small part of this unstable outflow is within the Compton thick region with $\log N_{\rm H} > 24$ (portions below the line marking the low angle $i = 11.9°$).

winds flow close to the disk surface at low equatorial angles. In this paper we investigate whether magneto-centrifugal outflows (Ferreira 1997; Casse & Ferreira 2000b) can reproduce the observed winds in terms of the correct range of ionization parameter (ξ), column density ($N_{\rm H}$), velocity ($v_{\rm obs}$), and density $n_{\rm H}$. The investigations are performed as a function of the two key accretion disk parameters, the disk aspect ratio ε and the radial exponent p of the accretion rate ($\dot{M}_{\rm acc} \propto r^p$). We also test whether our theoretical models can match the state dependant and angle dependant nature of the accretion disk winds. The results of our study are listed below:

- The cold solutions, which are solely driven by the magnetic acceleration, produce very narrow regions of detectable wind from the outer parts ($\geq 2.51 \times 10^5 r_{\rm g}$) of the accretion disk. In addition, the cold MHD winds have lower density ($\log n_{\rm H} \leq 9.9$) than predicted by observations. The winds were found to be equatorial within $i \sim 30°$ of the accretion disk surface.
- We realized that we need high values of $p(>0.04)$ to reproduce winds that can match observations. However p cannot be increased to desirable values in the framework of the cold MHD solutions. We definitely need warm MHD solutions to explain the observational results. In the warm MHD solutions, some extra heating at the disk surface causes a larger mass loading at the base of the outflow, which is then magnetically accelerated to form a denser wind. We speculate that the aforementioned heating may be due to the illuminating SED, particularly in the Soft state, or due to dissipation of energy by MHD turbulence within the disk. Even a small percent of the released accretion energy (if it were deposited on the disk surface, leading to local heating there, instead of being dissipated deep within the disk layers), would be enough to give rise to such warm MHD winds. Whether or not MHD turbulence in accretion disks provides such a surface heating is an open theoretical issue.
- In the Soft state, our densest warm MHD solution predicts a wind at $7.05 \times 10^4 r_{\rm g}$ with a density of $\log n_{\rm H} = 11.1$. The densest part of the wind ($\log n_{\rm H} > 8$) still remains equatorial within $i \sim 30°$ of the accretion disk. The values of the physical parameters are consistent with some of the observed winds in BHBs. However, there are some other extreme observations (e.g. GRO J1655-40; Miller et al. 2008) that require a denser wind at a smaller distance to the black hole. From our work we understand what kind of MHD solutions can reproduce such extreme winds: warm MHD solutions with $p \simeq 0.5$. It was beyond the scope of this paper to produce these particular solutions; however, we will generate and report them in our future publications where we will attempt to reproduce spectra of BHB winds of different kinds.
- The outflow illuminated by a Hard SED will not produce detectable wind because (i) the allowed region of the winds is smaller than the Soft SED case and (b) the wind region falls within the thermodynamically unstable range of $\log \xi$ and hence is unlikely to be detected.
- Thus, in the framework of MHD outflows we can satisfy the observed trends reported in Ponti et al. (2012, and references therein) that (a) winds are observed in the Soft states of the BHB outbursts (and are not expected in the Hard states); and (b) accretion disk winds in BHBs are equatorial. We were able to reproduce the expected values (consistent with observations) of distance, density, and velocity for the average winds in BHBs. For the extremely dense winds (and so at small distances from the black hole) our rigorous analysis was capable of pointing to the kind of accretion disks which will be able to reproduce them.

Acknowledgements. The authors acknowledge funding support from the French Research National Agency (CHAOS project ANR-12-BS05-0009 http://www.chaos-project.fr) and CNES.

References

Arnaud, K. A. 1996, ASP Conf. Ser., 101, 17
Blandford, R. D., & Payne, D. G. 1982, MNRAS, 199, 883
Blum, J. L., Miller, J. M., Cackett, E., et al. 2010, ApJ, 713, 1244
Casse, F., & Ferreira, J. 2000a, A&A, 353, 1115
Casse, F., & Ferreira, J. 2000b, A&A, 361, 1178
Chakravorty, S., Kembhavi, A. K., Elvis, M., & Ferland, G., & Badnell, N. R. 2008, MNRAS, 384, 24
Chakravorty, S., Kembhavi, A. K., Elvis, M., & Ferland, G. 2009a, MNRAS, 393, 83
Chakravorty, S., Misra, R., Elvis, M., Kembhavi, A. K., & Ferland, G. 2009b, MNRAS, 393, 83
Chakravorty, S., Lee, J. C., & Neilsen, J. 2013, MNRAS, 436, 560
Contopoulos, J., & Lovelace, R. V. E. 1994, ApJ, 429, 139
Diaz Trigo, M., Miller-Jones, J. C. A., Migliari, S., Broderick, J. W., & Tzioumis, T. 2013, Nature, 504, 260
Ferland, G. J., Korista, K. T., Verner, D. A., et al. 1998, PASP, 110, 761
Ferreira, J. 1997, A&A, 319, 340
Ferreira, J., & Casse, F. 2004, ApJ, 601, L139
Ferreira, J., & Pelletier, G. 1993, A&A, 276, 625
Ferreira, J., & Pelletier, G. 1995, A&A, 295, 807
Ferreira, J., Petrucci, P.-O., Henri, G., Saugé, L., & Pelletier, G. 2006, A&A, 447, 813
Frank, J., King, A., & Raine, D. 2002, Accretion Power in Astrophysics, 3rd edn. (Cambridge: Cambridge Univ. Press)
Fukumura, K., Kazanas, D., Contopoulos, I., & Behar, E. 2010a, ApJ, 715, 636
Fukumura, K., Kazanas, D., Contopoulos, I., & Behar, E. 2010b, ApJ, 723, L228
Fukumura, K., Tombesi, F., Kazanas, D., et al. 2014, ApJ, 780, 120
Fukumura, K., Tombesi, F., Kazanas, D., et al. 2015, ApJ, 805, 17
Garcia, P. J. V., Ferreira, J., Cabrit, S., & Binette, L. 2001, A&A, 377, 589
Higginbottom, N., & Proga, D. 2015, ApJ, 807, 107
Kallman, T. R., Bautista, M. A., Goriely, S., et al. 2009, ApJ, 701, 865
King, A. L., Miller, J. M., Raymond, J., et al. 2012, ApJ, 746, L20
Kubota, A., Dotani, T., Cottam, J., et al. 2007, PASJ, 59, 185
Lee, J. C., Reynolds, C. S., Remillard, R., et al. 2002, ApJ, 567, 1102
Mitsuda, K., Inoue, H., Koyama, K., et al. 1984, PASJ, 36, 741
Makishima, K., Maejima, Y., Mitsuda, K., et al. 1986, ApJ, 308, 635
Miller, J. M., Raymond, J., Fabian, A. C., et al. 2004, ApJ, 601, 450
Miller, J. M., Raymond, J., Homan, J., et al. 2006, ApJ, 646, 394
Miller, J. M., Raymond, J., Reynolds, C. S., et al. 2008, ApJ, 680, 1359
Miller, J. M., Raymond, J., Fabian, A. C., et al. 2012, ApJ, 759, L6
Neilsen, J., & Homan, J. 2012, ApJ, 750, 27
Neilsen, J., & Lee, J. C. 2009, Nature, 458, 481
Neilsen, J., Remillard, R. A., & Lee, J. C. 2011, ApJ, 737, 69
Peterson, B. M. 1997, An Introduction to Active Galactic Nuclei (Cambridge: Cambridge Univ. Press)
Petrucci, P.-O., Ferreira, J., H., Gilles, M., J., & Foellmi, C. 2010, A&A, 522, A38
Ponti, G., Fender, R. P., Begelman, M. C., et al. 2012, MNRAS, 422, L11
Ponti, G., Munoz-Darias, T., & Fender, R. P. 2014, MNRAS, 444, 1829
Remillard, R. A., & McClintock, J. E. 2006, ARA&A, 44, 49
Schulz, N. S., & Brandt, W. N. 2002, ApJ, 572, 971
Tarter, C. B., Tucker, W., & Salpeter, E. E. 1969, ApJ, 156, 943
Ueda, Y., Murakami, H., Yamaoka, K., Dotani, T., & Ebisawa, K. 2004, ApJ, 609, 325
Ueda, Y., Yamaoka, K., & Remillard R. A. 2009, ApJ, 695, 888
Ueda, Y., Honda, K., Takahashi, H., et al. 2010, ApJ, 713, 257

Appendix A: Cold versus warm disk wind solutions

In this appendix, we highlight some important points that can distinguish between "cold" and "warm" wind solutions from near-Keplerian accretion disks. In the terminology of Blandford & Payne (1982), a cold wind refers to a flow where the enthalpy is negligible with respect to the magnetic energy density at the base, namely at the disk surface. Unless some additional heating source occurs within the disk layers and/or at its surface, the temperature of the flow leaving the disk is at most comparable to that prevailing at the disk mid-plane. This translates into an enthalpy that is roughly $(h/r)^2$ times the gravitational potential, hence negligible in a thin disk. As a consequence, a wind with a positive Bernoulli integral can only be achieved by magnetic means. Cold models have been thus computed using different prescriptions for the thermal state of the magnetic surfaces: either isothermal (constant temperature along a surface, e.g. Ferreira (1997)) or adiabatic surfaces (decreasing temperature, e.g. Casse & Ferreira 2000a).

On the contrary, warm disk wind models rely on the existence of an ad hoc entropy generation term Q. The exact energy equation for the outflowing material writes

$$\rho T \frac{\mathrm{d}S}{\mathrm{d}t} = \rho T \boldsymbol{u}_\mathrm{p} \cdot \boldsymbol{\nabla} S = Q_\mathrm{real}, \tag{A.1}$$

where S is the specific entropy and Q_real is the local source of entropy that arises from the difference between all heating and cooling processes (Casse & Ferreira 2000b). More specifically, it can be written $Q_\mathrm{real} = (\Gamma_\mathrm{eff} + \Gamma_\mathrm{turb} + \Gamma_\mathrm{ext}) - (\Lambda_\mathrm{rad} + \Lambda_\mathrm{turb})$, where $\Gamma_\mathrm{eff} = \eta_m J_\phi^2 + \eta'_m J_\mathrm{p}^2 + \eta_v r |\boldsymbol{\nabla}\Omega|^2$ is the effective Joule and viscous heating; Γ_turb is a turbulent heating term that cannot be described by simple anomalous transport coefficients (namely the term Γ_eff) and would correspond, for instance, to some resonant or wave heating above the disk; and Γ_ext is an external source of energy (typically due to some illumination by UV or X-rays, if present at all). $\Lambda_\mathrm{rad} = \boldsymbol{\nabla} \cdot \boldsymbol{S}_\mathrm{rad}$ is the radiative cooling ($\boldsymbol{S}_\mathrm{rad}$ being the radiative flux) and Λ_turb is the cooling due to turbulent energy transport, which is most probably also taking place inside turbulent disks (see Casse & Ferreira (2000b) for more details).

Taking into account all these processes is a tremendous task which requires the understanding not only of MHD turbulence in outflow emitting disks, but also of the complex radiative processes at work in various astrophysical objects. A simplified approach is actually to assume the entropy generation term, which is what we do. The above exact energy equation follows the flow streamlines, which is inconvenient to use when integrating the equations from the disk mid-plane to outflow asymptotics (isothermal solutions cannot be obtained for instance). Instead, the energy equation actually solved is

$$\frac{\rho u_\mathrm{p}}{B_\mathrm{p}} \boldsymbol{B}_\mathrm{p} \cdot \nabla C_\mathrm{s}^2 = (\gamma - 1) \left(Q + C_\mathrm{s}^2 \frac{\rho u_\mathrm{p}}{B_\mathrm{p}} \boldsymbol{B}_\mathrm{p} \cdot \nabla \ln \rho \right), \tag{A.2}$$

where γ is the adiabatic index and $C_\mathrm{s}^2 = P/\rho$ with a prescribed self-similar function Q described in Sect. 4.1 of Casse & Ferreira (2000b). This equation is strictly equivalent to Eq. (A.1) in the ideal MHD outflow region and allows the disk vertical structure to be treated. Once a full trans-Alfvénic MHD flow solution is obtained, the real entropy generation term Q_real can be computed using Eq.(A.1) as shown in Fig. A.1.

To illustrate cold and warm solutions, we choose two representative super-Alfvénic solutions with the same $\varepsilon = 0.01$. The cold solution is isothermal ($\gamma = 1$) with $p = 0.006$, whereas the warm solution with $\gamma = 5/3$ has $p = 0.1$ and requires a heating function Q. The upper panels of Fig. A.1 show, for both solutions, the vertical profiles along a magnetic surface of the effective turbulent heating Γ_eff and the imposed Q, as well as the real Q_real entropy generation terms. The entropy parameter, defined as

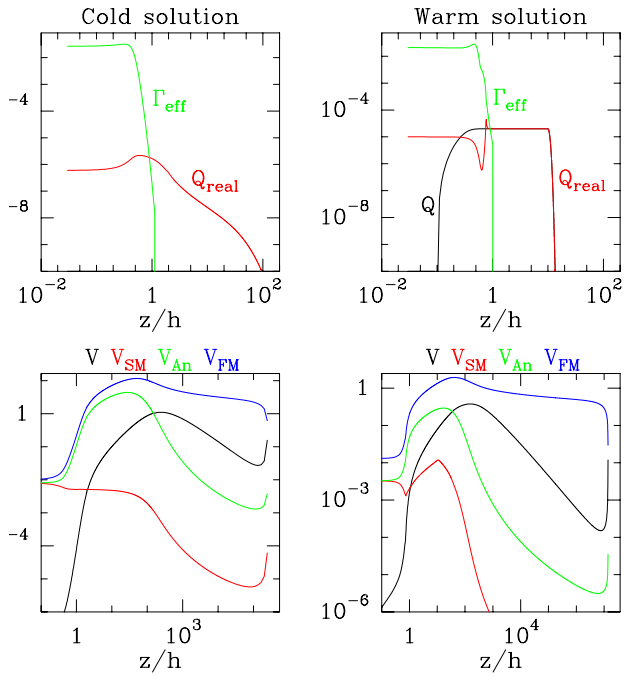

Fig. A.1. Profiles along a magnetic surface of a typical cold isothermal solution with $p = 0.006$ (*left*) and warm solution with $p = 0.1$ (*right*). *Top*: effective turbulent heating Γ_eff, real entropy generation term Q_real, and prescribed function Q in arbitrary units. *Bottom*: critical velocities (see text) normalized to the disk mid-plane sound speed.

$$f = \frac{\int_V Q_\mathrm{real} \mathrm{d}V}{\int_\mathrm{disk} \Gamma_\mathrm{eff} \mathrm{d}V}, \tag{A.3}$$

where the volume V is both the disk and the wind, can be computed a posteriori once a solution is found. It provides the ratio of the power due to the extra heating going into the wind to the turbulent power dissipated within the disk. The warm solution resulted in an entropy parameter $f = 0.02$, which suggests that local MHD turbulence could actually lead to such a solution. Indeed, the required extra heating only amounts to 2% of the power that would be dissipated within the disk (hence a reduction of 2% in the disk luminosity). This would be possible if MHD turbulence itself ($(\Gamma - \Lambda)_\mathrm{turb}$ terms) conveys that power to the disk upper layers (the "base of the wind"). This is an open theoretical issue, of course. If such a process proves to be nonexistent, then one should only rely on illumination (Γ_ext term) to obtain warm MHD solutions of this kind. We note that magneto-centrifugal winds undergo a huge adiabatic cooling at the disk surface so that to remain isothermal requires some heat deposition as well. Thus, the cold solution given here would require a Q_real such that $f = 1.6 \times 10^{-3}$. The lower panels show the profiles of the various velocities relevant in such MHD flows: the critical flow speed V, the slow V_SM and fast V_FM magnetosonic phase speeds, and the Alfvén speed V_An (see Ferreira 1995 for their meaning and definition). We note that the warm solution becomes super-SM (super-slow magnetosonic) above the disk, but that V_SM is always smaller than the local sound speed.

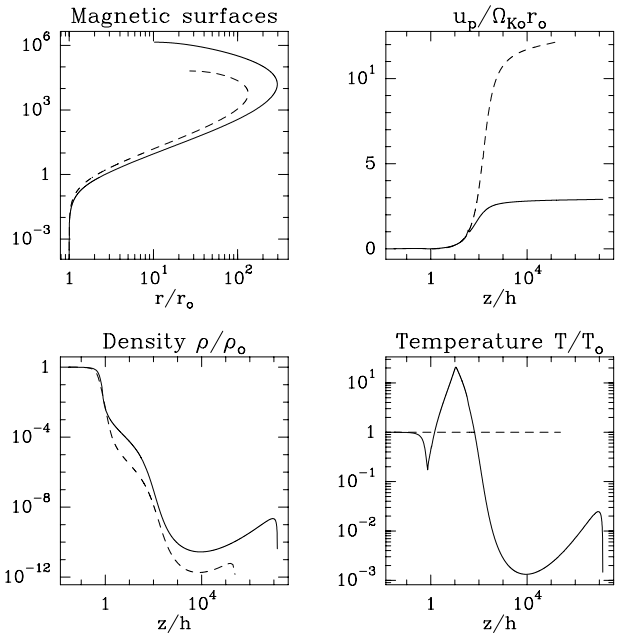

Fig. A.2. Shape of the magnetic surfaces (*top left*) and vertical profiles along the magnetic surfaces of **a)** outflow poloidal velocity normalized to the Keplerian speed at the field line anchoring radius r_o (*top right*); **b)** density normalized to its mid-plane value (*bottom left*); and **c)** temperature normalized to its mid-plane value (*bottom right*). Solid lines are for the warm solution, dashed for the isothermal.

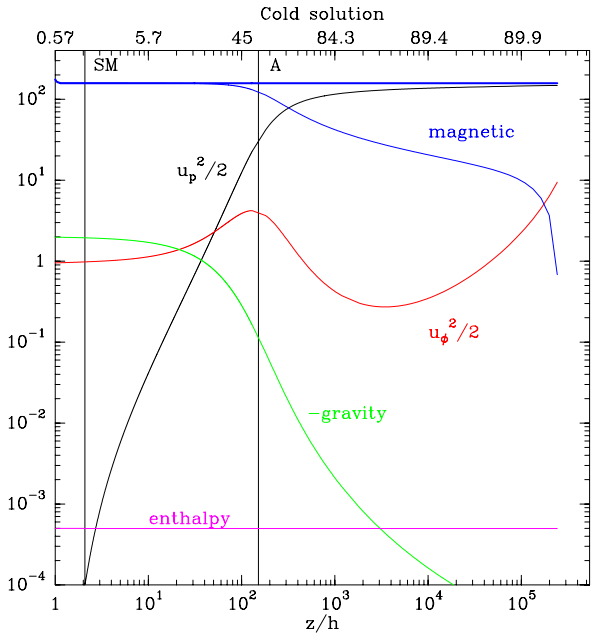

Fig. A.3. Profiles of various specific energy reservoirs (in units of $GM/2r_o$) along a magnetic surface anchored at a radius r_o for the cold isothermal solution with $p = 0.006$. The SM point is located at $x_{SM} = z/h = 2.08$ and the Alfvén point at $x_A = 151.5$. The thick solid blue line is the sum of all terms and defines the Bernoulli invariant. At the *top of the figure*, the axis is labelled with the inclination angle (in degrees) from the disk mid-plane $i = \mathrm{atan}(\varepsilon z/h)$.

The resulting solutions are shown in Fig. A.2. While the location of the SM point remains roughly above the disk surface in both cases ($x_{SM} = z/h = 2.08$ in the cold case, $x_{SM} = 1.1$ in the warm case), the main difference introduced by the surface heating term is the existence of a radial pressure gradient above the disk surface enforcing the wind to open up (Ferreira (2004)). Thus, while the Alfvén surface for the cold solution is located at $x_A = 151.5$, namely $z_A/r_o = 14.61$, $r_A/r_o = 9.64$, or an angle $\Phi_A = 33°$ from the vertical axis, it is much closer to the disk surface in the warm case with $x_A = 36.2$, namely $z_A/r_o = 0.92$, $r_A/r_o = 2.54$, or $\Phi_A = 70°$. However, the overall outflow behaviour remains the same; after an initial widening up to a maximum distance, the flow undergoes a recollimation towards the jet axis (perpendicular to the disk) where an oblique shock is expected to occur (and the validity of the self-similar solution breaks down, Ferreira 1997). Owing to the heating term present in the warm solution, the flow temperature is seen to increase up to about 20 times the mid-plane temperature before undergoing an adiabatic decrease once the heating vanishes ($Q = 0$). We note that the temperature profile mostly affects the disk vertical balance, allowing thereby a larger mass loss (larger ejection index p) in the warm case than in the isothermal case; however, the asymptotic outflow speed is mainly a result of the magnetic energy (dominant term) conversion. This is illustrated in Figs. A.3 and A.4, which show for the cold and warm cases, respectively, the profiles of the various specific energy reservoirs along a magnetic surface (the sum of which defines the Bernoulli invariant). In self-similar solutions of this kind, all the initial magnetic energy is eventually converted into outflow kinetic poloidal energy.

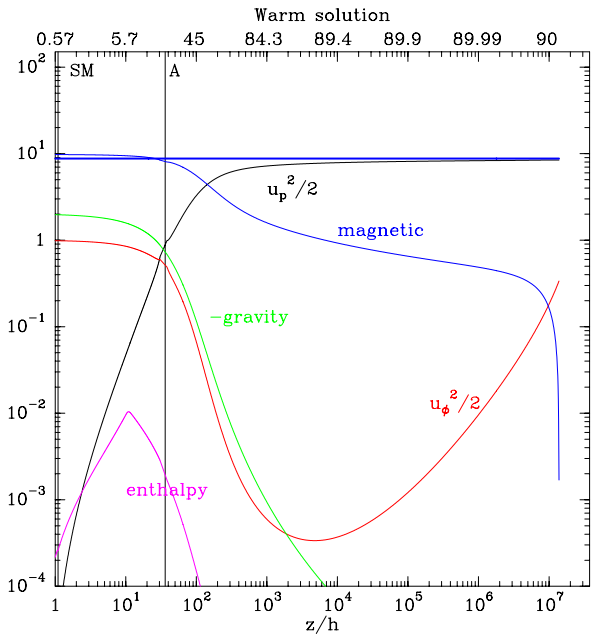

Fig. A.4. Same as Fig. A.3, but for the best warm solution ($\varepsilon = 0.01$, $p = 0.1$). The SM point is located at $x_{SM} = 1.1$ and the Alfvén point at $x_A = 36.2$. We note the drastic decrease in the enthalpy due to the adiabatic cooling once the heating term vanishes.